

Optimal Design of 50kW Concentrated Winding Bearingless Motor

Ye gu Kang

Dept. of Mechanical Engineering
University of Wisconsin-Madison
Madison, USA
ykang22@wisc.edu

Eric L. Severson

Dept. of Electrical and Computer Engineering
University of Wisconsin-Madison
Madison, USA
eric.severson@wisc.edu

Abstract—Bearingless motor technology offers an integrated and compact alternative to active magnetic bearings for developing contact-free and oil-free industrial compressor systems. These systems require high speed motors designed for significant power levels. This paper considers the optimal design of a 50kW, 30,000 r/min bearingless motor. This design is based around a topology with a fractional slot-concentrated winding and a surface mount permanent magnet motor (the popular 4-pole, 6-slot design), making it a practical and potentially cost-effective design to manufacture. A parallel no voltage combined winding is designed so that the same coils that create torque can also be used to create suspension forces. The rotor magnets are retained via a carbon fiber banding, which is designed within the proposed optimization process. A multi-physics design framework is developed based around the differential evolution algorithm that considers both the electromagnetic design and the structural integrity of the rotor. Design metrics unique to bearingless motors are described and implemented. The final design achieves a maximum efficiency of nearly 96%, a safety factor of approximately 2 in the rotor structural analysis, and is able to support the rotor weight with only 2.5% of the rated armature current.

Index Terms—Bearingless motor, Self-bearing motor, Magnetic levitation, Multi-Physics, Optimization, Differential evolution

NOMENCLATURE

D_{os}	Outer stator diameter (mm)
D_{or}	Outer rotor diameter (mm)
E	Young's modulus
E_a	Force angle error (degrees)
E_m	Force amplitude error normalized by desired force magnitude
FRW	Force per unit of rotor weight
L_g	Airgap length (mm)
L_r	Distance from rotor tooth radius to magnet radius (mm)
L_{st}	Stack length (mm)
O_m	Objective function variable m
P_a	Penalty function
PR	Pole arc ratio
Q	Number of stator slots
SR	Slot ratio
S_1	Shoe height 1 (mm)
S_2	Shoe height 2 (mm)
SF	Safety factor
T_b	Sleeve thickness (mm)

T_m	Permanent magnet thickness (mm)
T_r	Torque ripple normalized by average torque
TRV	Torque per unit of rotor volume
T_s	Stator yoke thickness (mm)
W_t	Tooth width (mm)
w_m	Weighting factor for objective function variable m
η	Machine efficiency
ν	Poisson's ratio
ρ_m	Mass density of materials (kg/m ³)
σ_y	Yield stress
σ_m	Maximum working stress

I. INTRODUCTION

For high speed and large power applications, active magnetic bearings (AMB) are an attractive solution to provide contact-free support for motor shafts. However, combining a motor with AMBs results in a large and expensive system due to the use of additional power electronics and separate electromechanical actuators for torque and radial forces [1], [2]. Bearingless motors integrate the functionality of a magnetic bearing and a motor into a single electric machine [1], and therefore present a more integrated solution with the potential to solve the shortcomings of AMB-based systems.

Bearingless motor technology has been considered and successfully commercialized in several low power and niche applications, for example in artificial hearts and high purity pumps and mixing devices [1], [3]–[5]. Recently, several studies have considered higher power industrial compressor applications [6]–[10]. This has seen only limited success so far, with the largest experimental results that the authors are aware of being reported at approximately 30 kw [10], [11]. Part of the reason for this is lack of published literature on applying optimization algorithms to bearingless motors to achieve performance and efficiency levels suitable for high speeds. Literature on bearingless motor design is frequently limited to a design space exploration, where parameters are swept individually without any design optimization algorithm. Apart from being an inefficient approach to optimization, this technique won't take into account the non-linear and coupled nature of the parameters being optimized in the design process.

The primary contribution of this paper is to further develop a multi-variable FEA-based differential evolution (DE) algorithm to optimize the design of a large power bearingless motor. Specifically, the optimal design of a 50 kW, 30,000 r/min bearingless permanent magnet synchronous motor (BPMSM) is investigated for industrial compressor applications. Initial efforts to develop this optimization framework have been published in [12]. This paper is fundamentally different from the previous work by its inclusion of the rotor's structural modeling (a critical aspect of high speed machine design) in the optimization framework as well as considering a new rotor design that offers more flexibility to minimize suspension force ripple. In this paper, modeling details and an optimization strategy for combined structural and electromagnetic design are presented, with emphasis placed on aspects that are unique to high speed bearingless motors. A custom multi-objective function is designed based around minimizing torque and force ripple and maximizing efficiency, torque density, and force density.

II. MOTOR TOPOLOGY

This paper investigates the optimal design of a 6 slot, 4 pole permanent magnet motor as a bearingless motor. The stator winding of a conventional surface permanent magnet (SPM) motor is modified so that it produces a 2 pole suspension field in addition to the 4 pole field used to create torque. The flux paths for different excitation conditions are shown in Fig. 1. When the 4 pole motor fields (top right) are added to a 2 pole suspension field (bottom left), the resulting field distribution (bottom right) is concentrated on one side of the airgap, which creates a force vector in that direction. The suspension field can be rotated in the airgap to create a force vector in any direction. The motor winding responsible for creating these two airgap fields can be implemented as either two separate windings (a torque winding and a suspension winding) or as a single “combined” winding, where the same coils are used to create both suspension forces and torque. Examples of different winding configurations for the 6 slot, 4 pole design are summarized in [13].

In the separated winding design, the stator slot space is divided between the suspension and the torque windings. In typical designs, between 25% - 50% of the slot space is allocated to the suspension winding which decreases the torque rating of the motor by the same fraction [1], [8], [10], [14], [15]. In combined winding designs, since the same coils provide both torque and levitation forces, the bearingless motor drive is able to dynamically allocate the slot space between creating suspension forces and torque. This is a highly advantageous feature since most bearingless motors need very little suspension current to support the static loading of the machine (i.e., gravity), while transient conditions (i.e., passing through a critical speed) may briefly require significantly greater forces. During normal operation, when suspension force requirements are low, a combined winding bearingless motor will have nearly the same torque density as a non-bearingless motor.

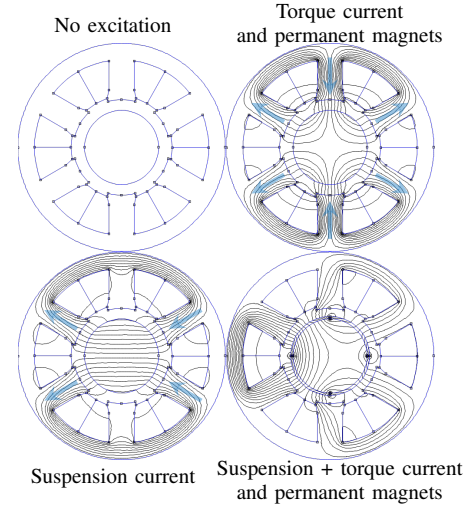


Fig. 1. Flux paths of the BPMSM under different excitation conditions

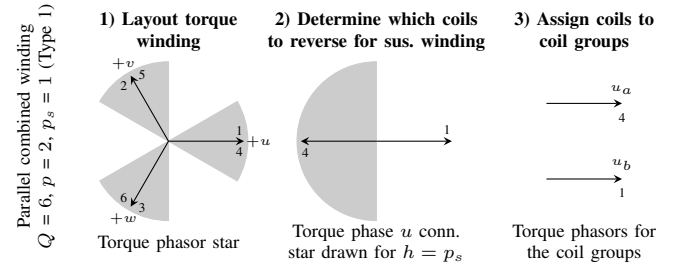


Fig. 2. Parallel DPNV winding design steps from [14] drawn for the BPMSM considered in this paper. The phasor numbers correspond to the coil numbers in Fig. 3

There are several fundamentally different approaches to combined bearingless windings known in the literature, for example [5], [16]–[18], each with differing requirements in terms of the power electronics. The authors of this paper propose implementing the combined winding of large power bearingless motors with parallel no voltage windings as they are able to use standard motor drive hardware, which is already available in the form of life-cycle tested and reliable products. General theory of operation of no voltage combined winding motor drives is presented in [18] and a step-by-step guide to designing the windings is presented in [14]. Control considerations for cross-coupling between suspension and torque operation are presented in [19].

The procedure presented in [14] is used to design the parallel winding used for the 6 slot, 4 pole bearingless motor. These steps are shown in Fig. 2 via the star of slots design method. The resulting concentrated winding layout is then shown in Fig. 3. The connections to the motor drive are shown in Fig. 4, where the dotted terminals correspond to the “+” terminals of Fig. 3. The motor and suspension inverters are responsible for regulating current that produces both torque and suspension forces. A detailed description of the current regulators is provided in [19].

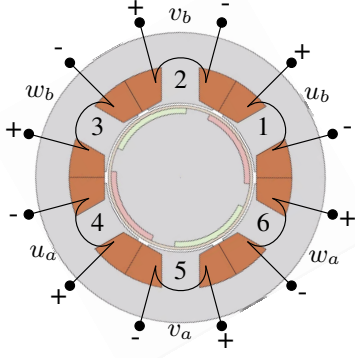


Fig. 3. Winding layout for the parallel no voltage combined winding. The “+” terminals correspond to the dotted terminals in Fig. 4.

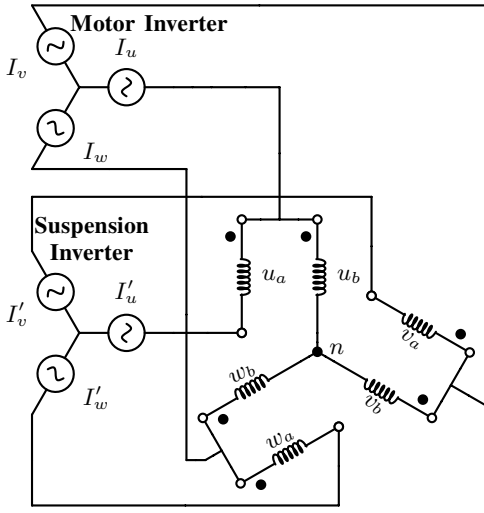


Fig. 4. Parallel DPNV combined winding [19]. The dotted terminals correspond to the “+” terminals in Fig. 3

III. MODELING

In a previous work [12], the authors have developed an optimization framework for the design of a 6 slot, 4 pole BPMSM design. This framework was based exclusively on the electromagnetic (EM) design using an open source static 2D FEA package (FEMM [20]). This paper builds on the previous framework by 1) considering a new rotor topology and 2) extending the framework to include structural stress analysis (ST) of the rotor integrity—a critical component of any high speed motor design. An overview of the machine model (both EM and ST) used in the multi-physics optimization process is now presented.

A. Electromagnetic

The rotor structure considered in this paper is depicted in Fig. 5 along with the dimensions that define its radial cross-section. From the EM perspective, the key difference between this rotor structure and the two structures considered in [12] is the inclusion of a variable height rotor tooth between the

permanent magnets (dimensioned as L_r in Fig. 5). This tooth has been added to give the design more freedom for tuning the airgap field harmonics to reduce force ripple while retaining high force and torque density. The design is determined by 10 independent geometric variables which are listed in Table V and most of which are labeled in Fig. 5. Note that SR and PR are defined by (1) and (2), where $\theta_s = 60^\circ$ (due to the stator having 6 slots) and $\theta_p = 90^\circ$ (due the rotor having 4 poles).

$$SR = \frac{\theta_t}{\theta_s} \quad (1)$$

$$PR = \frac{\theta_m}{\theta_p} \quad (2)$$

The EM evaluation is now briefly described with more detailed information provided in [12].

1) *Stack length*: The 2D FEA solver is used to evaluate torque and force density as unit length quantities. The axial stack length, L_{st} of the design is calculated as the value required to obtain the rated torque (15.9 Nm for the 30,000 r/min rated speed and 50 kW rated power). This calculation is shown in (3), where T_1 is the unit length torque value and the efficiency is approximated as $\eta = 96\%$.

$$L_{st} = \frac{P_r}{\omega_m \eta T_1} \quad (3)$$

2) *Torque performance*: Peak-to-peak torque ripple T_r and average torque divided by rotor volume TRV are the metrics used to assess the torque performance. These quantities are determined via static FEA solves as the rotor rotates in 10° increments over a 60° span at rated current.

3) *Loss and efficiency*: Iron, copper, magnet, and air friction loss are evaluated to determine the motor design's efficiency. Lamination iron loss calculations are made with the well-known Steinmetz Equation, using loss coefficients curve-fit to the material data sheet [21]. Copper losses are calculated as ohmic losses of each coil without ac effects and magnet eddy current losses are calculated using a function provided in FEMM. Air friction losses are calculated on the radial and axial surfaces of the rotor using calculations based on air friction coefficients as described in [22] and [23].

4) *Force evaluation*: Force ripple and average force divided by rotor weight FRW are the metrics used to assess the suspension force performance. Force ripple is decomposed into a force error angle and a force magnitude error. This is illustrated as an example in Fig. 6, where a desired force vector \vec{F}_c is along the x -axis, while the force that is actually produced \vec{F}_a at any given rotor angle consists of both x and y components. The magnitude error and error angle values are calculated as (4) and (5). These values are determined via FEA solves as the rotor rotates in 10° increments over a 180° span at rated current. Large force error angles can result in instability in the magnetic suspension control. For this reason, it is suggested in [7] that designs limit the maximum error angle to $E_a \leq 5^\circ$.

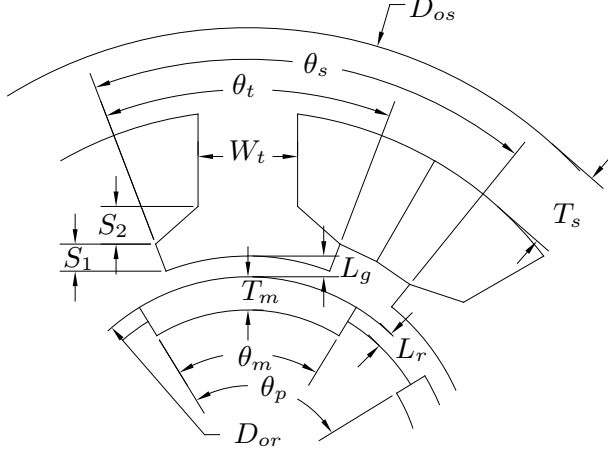


Fig. 5. Radial cross-section of the BPSM and relevant geometric variables.

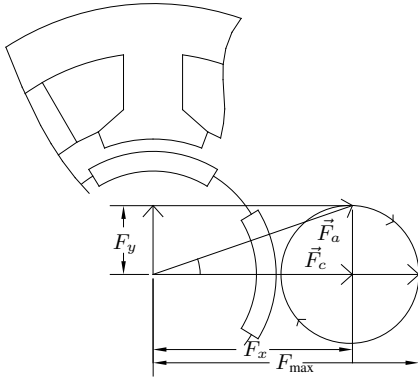


Fig. 6. Illustration of force angle and amplitude error.

$$E_m = \frac{F_{max} - F_x}{F_x} \quad (4)$$

$$E_a = \tan^{-1} \left(\frac{F_y}{F_x} \right) \quad (5)$$

B. Structural

To obtain high torque density values, high surface velocities at the outer diameter of the rotor are required. Conventional surface mount permanent magnet rotor designs rely on a retaining sleeve to support the magnets. This is because the contact force of adhesives is not strong enough to withstand the centrifugal forces and sintered NdFeB magnets' ultimate tensile strength (typically 80 MPa) is not high enough to withstand the tensile stress. This investigation considers the use of a carbon-fiber banding to fix NdFeB magnets to the rotor surface. The structural design analysis presented in [24] is followed. Two criteria must be met to maintain rotor structure integrity: first, the tensile yield strength of the sleeve has to be greater than the tangential pre-stress combined with

the tangential stresses due to centrifugal forces—see (6). This is to avoid permanent deformation of the sleeve. Second, the sleeve must maintain radial contact pressure on the magnet over the entire speed range. To satisfy this condition, contact pressure from pre-stressing the sleeve must be greater than radial centrifugal forces produced by the magnet and sleeve at maximum speed—see (7). This is to avoid the magnet slipping from the rotor under load. For both of these criteria, the maximum speed is taken as 1.2 times the rated speed.

$$\sigma_{y,s} > \sigma_{\text{prestress},s} + \sigma_{\omega} \quad (6)$$

$$p_{c,\text{prestress}} > p_{\omega,m} + p_{\omega,s} \quad (7)$$

In this paper, the sleeve is always assumed to have a maximum thickness, which is constrained by the spacing between the magnet surface and stator based on (8).

$$T_b = L_g - 0.3 \quad (8)$$

To obtain the needed pre-stress on the magnets, the sleeve's inner diameter is undersized as compared to the magnet diameter by ΔD , shown in Fig. 7. This undersize is calculated by (9), where a simplified thin cylinder is assumed, ρ is the density of the material (shown in Table IV), ω_o is 1.2 times the rotor rated speed in rad/s, and r_s and r_m represent the average radius of sleeve and PM.

$$\Delta D = (p_{\omega,m} + p_{\omega,s}) \frac{(D_{or} + 2T_b)r_s}{ET_s} \quad (9)$$

$$p_{\omega,m} = r_m \rho_m \omega_o^2 T_m \quad (10)$$

$$p_{\omega,s} = r_s \rho_s \omega_o^2 T_s \quad (11)$$

The stress analysis of the rotor at maximum speed is evaluated using 2D FEA of the geometry shown in Fig. 7. Depending on the design variables L_r and PR , the rotor may have an inter-pole gap, which is expected to result in additional bending stresses at the magnet edges. The maximum stress of the rotor is evaluated by the von-Mises criterion, where irreversible damage to the rotor will occur when the von-Mises stress exceeds the yield strength of the sleeve. A safety factor (12) is used in the optimization, with a penalty assigned to designs with $SF < 1.5$.

$$SF = \frac{\sigma_y}{\sigma_m} \quad (12)$$

IV. OPTIMIZATION

The popular differential evolution (DE) algorithm is used to optimize the BPMSM design. The algorithm generates BPMSM design parameters from which the EM and ST FEA models are automatically created and evaluated. A flow chart of the optimization process is shown in Fig. 8. A multi-objective function is used to assess each design. This function is defined in (13) and consists of a penalty P_a , objective variables O_m , and weighting factors w_m . The penalty is used to eliminate designs that either violate the geometric constraints of Table II or violate the requirement of $SF \geq 1.5$.

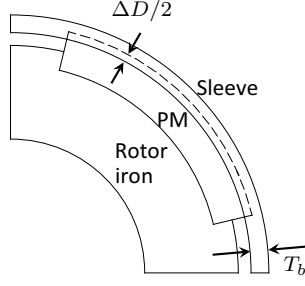


Fig. 7. BPMSM rotor geometry

The objective variables are scaled performance variables and are defined in Table I along with weighting factors. The scaling of the performance variables is set up to normalize the objective variables of a “reasonable” design about 1 (i.e. T_r is scaled by $1/0.05$, because 5% torque ripple is deemed a reasonable value). This allows the weighting factors to be defined based on the importance of each performance variable.

$$MO = P_a + \sum_{m=1}^6 O_m w_m \quad (13)$$

The materials used for the EM analysis are listed in Table III. Rated stator coil currents are modeled which produce simultaneous suspension forces and torque. This is done by assigning the rated current density to the coils, but allocating 2.5% of the current density to suspension forces and the remaining 97.5% to q -axis torque current. The performance variables are calculated from the 2D FEA field results as described in Section III-A.

The material properties used for the structural analysis are determined in [24]–[26] and are summarized in Table IV. The composite banding thickness and undersize are determined from the design variables as described in (8) and (9). The ST models are evaluated at rated rotational speed (30,000 r/min) using quarter symmetry, as depicted in Fig. 7 and with a surface-to-surface contact pair between the magnet and both the rotor and sleeve.

The FEA models are evaluated in parallel reduce the design time. Note that in this design process, D_{os} is assigned a fixed value. This is done to constrain the size of the design space and allow more insightful design trends to be observed from the optimization results. More detailed information on the optimization framework can be found in [12].

V. OPTIMIZATION RESULTS

The optimization framework was run with a population of 12 for 100 iterations, resulting in 1200 designs being generated and evaluated by FEA. The design parameters of the best design are presented in Table V and the geometry is shown in Fig. 9. Interestingly, the BPMSM design converged to an open slot shape (no tooth tips) with a short effective airgap

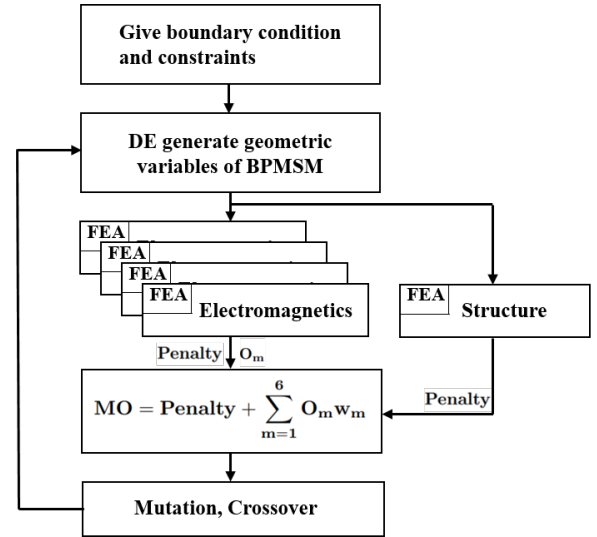


Fig. 8. FEA based DE optimization process.

TABLE I
OBJECTIVE VARIABLES AND WEIGHTING FACTORS

Symbol	Meaning	Symbol	Weighting factor
O_1	$30e3/TRV$	w_1	1
O_2	$1/FRW$	w_2	1
O_3	$T_r/0.05$	w_3	0.1
O_4	E_a	w_4	0.1
O_5	$E_m/0.05$	w_5	0.1
O_6	$1/\eta^2$	w_6	10

TABLE II
GEOMETRIC CONSTRAINTS

Symbol	Min. value [mm]	Max. value [mm]	Initial value [mm]
D_{os}	250	250	250
D_{or}	75	100	80
L_g	2.5	9	6
T_m	2	8	4
W_t	20	40	35
T_s	15	35	20
S_1	3	10	5
S_2	3	10	5
SR	0.5	0.9	0.7
PR	0.6	0.9	0.7
L_r	0	8	3

TABLE III
EM DESIGN INFORMATION

Permanent magnet	N40H
Laminations	Arnon5
Lamination Stacking Factor	0.91
Conductor Current Density	$3.7A_{rms}/mm^2$
Slot packing factor	0.45
Rated Power	50 kW
Rated Speed	30,000 r/min

TABLE IV
MATERIAL PROPERTY FOR STRESS ANALYSIS

	ρ [kg/m ³]	E [MPa]	ν	σ_y [MPa]
PM	7350	160	0.24	—
Sleeve	1550	186.2	0.3	1100
Rotor iron	7560	210	0.3	400

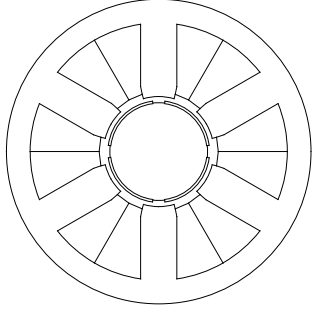


Fig. 9. Optimized design geometry.

length. The final design can support the rotor's weight with 2.5% of rated current used for suspension forces and has a maximum error angle of only 1.1° at rated load. Details of the electromagnetic and structural design optimization are now described.

A. Electromagnetic design

The geometric input variables and the performance variables of the best design of each iteration are shown in Fig. 11. The slot ratio SR determines the amount of tooth tip that is present, and is known to have a strong influence on the slotting effect for torque ripple. This variable converged to a value of 0.5, which corresponds to a design without tooth tips. Designs without tooth tips or minimal tooth tips (small

TABLE V
OPTIMIZED DESIGN GEOMETRIC AND PERFORMANCE VARIABLES

Input variable	Value [mm]	Performance variable	Value
D_{or}	83.4	TRV	41.0
L_g	3.5	FRW	1.0
T_m	2.1	T_r^a	6.9
W_t	29.7	E_a^b	1.1
T_s	19.4	E_m^a	2.3
S_1	6.4	η^b	95.6
S_2	3.7		
SR	0.54		
PR	0.84		
L_r	1.6		
L_{st}	62.7		

^ain %

^bin degrees

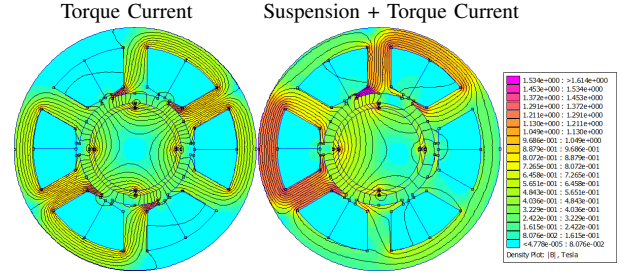


Fig. 10. Regional saturation with rated torque current (left) and with rated torque and force current (right) for a slot ratio of $SR = 0.85$.

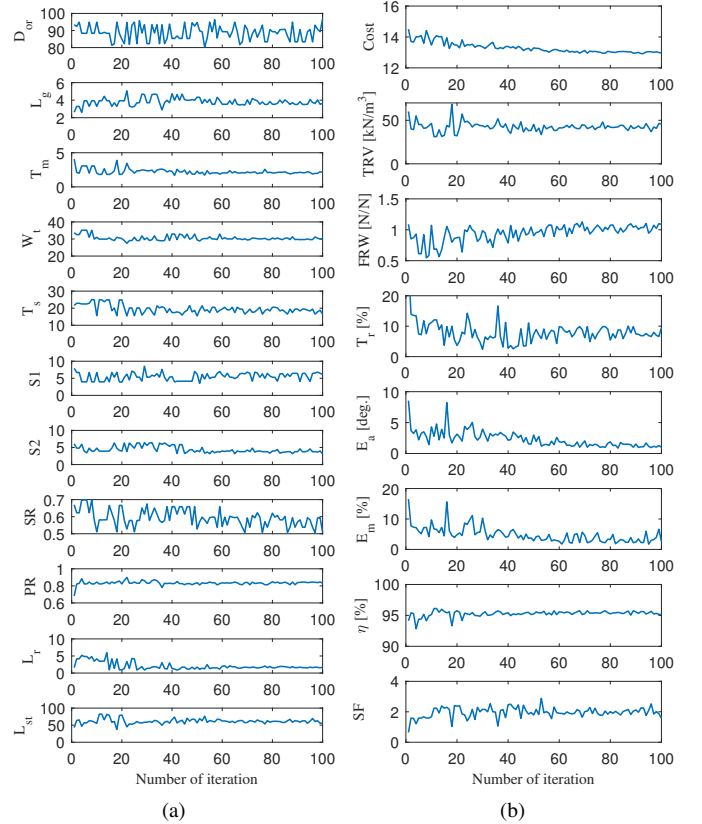


Fig. 11. Optimal design values in each iteration: (a) geometric variables; (b) performance variables

values of SR) are typically advantageous for force ripple because they eliminate areas of localized saturation. Since the suspension field has a different number of poles as compared to the rotor, its field rotates at a different speed compared to the magnetizing field of the motor. An example of saturated tooth tips due to torque excitation as compared to torque + suspension current excitation is shown in Fig. 10.

Fig. 11(a) shows that the rotor diameter D_{or} was varied over a broad range during the design process. This input variable has a strong influence over the magnet volume and, in this framework where the stator diameter D_{os} is held to a constant value, it also has a strong influence on the slot size. This means that D_{or} is strongly coupled to the magnetic

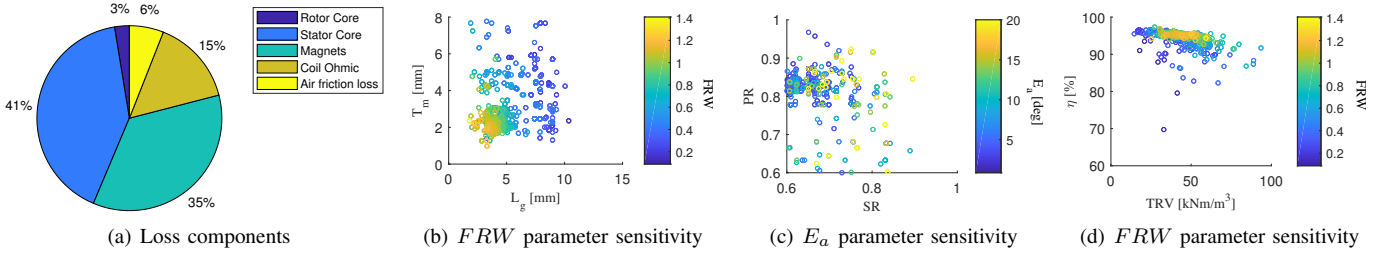


Fig. 12. Optimal design EM analysis results: (a) loss components at rated speed (30,000rpm) and rated load (50 kW); (b)-(d) parameter sensitivity plots relating design variables to EM performance variables

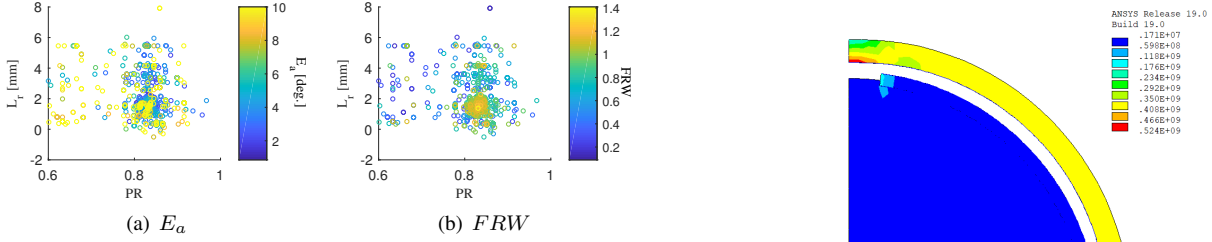


Fig. 13. Parameter sensitivity of the rotor tooth offset L_r

and electric loading, which determine the airgap shear stress (and therefore torque and force density). Further, the radial surface windage losses are proportional to D_{or}^4 [12] and, since the rated rotational speed is fixed, the centrifugal loading increases with increasing D_{or} . All of these dependencies have conflicting impact on the various performance variables, causing D_{or} to fluctuate broadly over the optimization process.

The loss distribution of the best design is shown in Fig. 12(a) at rated speed and load. The PM loss and stator loss are the two dominant loss components. When looking at this in terms of loss density, the magnet loss density is very high and will need to be properly cooled in order to make this a practical design. Future work on this topology will take thermal modeling into consideration and possibly investigate techniques to reduce magnet losses (i.e., segmented magnets).

The suspension force performance is a consideration that is unique to bearingless motors. Fig. 12(b) shows the improvement on FRW with small effective airgap (thin magnets and a small physical airgap). The force per rotor weight ratio FRW scales similarly to the torque per rotor volume ratio TRV as a function of the electric and magnetic loading (airgap shear stress) and the rotor volume. Torque ripple and force error terms are highly dependent on the harmonic content in the airgap, which is impacted by several variables, namely SR , PR , $S1$, $S2$, T_m , L_g , L_r . The concentration of SR and PR in Fig. 12(c) indicates that a certain combination of SR and PR are preferred for E_a optimization. Fig. 12(d) is a pareto plot that shows trade-off of performance variables TRV and η . Using more material to design a large size machine can improve η at the expense of a lower TRV value. Interestingly, FRW shows no such trade-off relationship with η . Similar to TRV , the largest FRW values are found for small effective airgap length (to obtain high airgap flux density). However,

Fig. 14. FEA stress analysis of optimal design at rated speed.

TRV is highest with large values of SR , while FRW is highest for low values of SR .

As compared to previous literature, this paper has considered the addition of a variable height rotor tooth between rotor magnets. The height of this tooth relative to the magnet outer radius L_r converged to 1.6 mm, which results in a partial rotor tooth. It is interesting to observe in Fig. 13(b) that the force per rotor weight FRW prefers a narrow range of this value, outside of which FRW is decreased. Fig. 13(a) shows both low and high force angle error E_a in the converged region, which indicates that E_a is a function of many other geometric variables as well. From this analysis, it can be concluded that L_r gives the design algorithm more flexibility to maximize FRW .

B. Structural design

Results of the stress analysis of the optimal rotor design are depicted in Fig. 14. As described in Section III-B, the composite banding is designed to pre-stress the magnet and additional stress components arise with centrifugal loading. The anticipated additional stress due to the sleeve bending at the edge of the magnet is also apparent.

The sensitivity of the safety factor SF to rotor diameter D_{or} , the magnet thickness T_m , and the pole arc ratio PR is depicted in Fig. 15. Since the designs are all evaluated at the same speed, the maximum tangential stress is proportional to D_{or}^2 and increases with the thickness (mass) of the magnets—which is clearly confirmed by the impact of these variables on SF in Fig. 15(a). Decreasing values of PR correspond

to increasing bending stresses in the sleeve due to larger gaps between the magnets, which decreases the value of SF and is clearly confirmed in Fig. 15(b). From the structural design perspective, a value of $PR = 1$ is preferred to eliminate bending stress. However, as previously described, the suspension force characteristics prefer a smaller PR value.

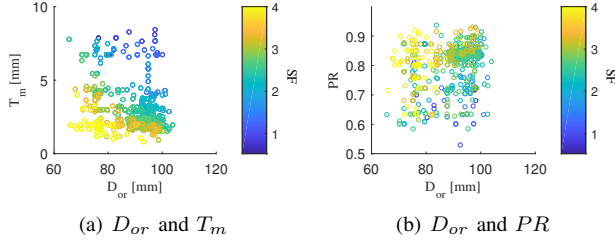


Fig. 15. Parameter sensitivity of the safety factor

VI. CONCLUSION

In this paper, a multi-objective optimization framework is developed and used to optimize the design of a 50 kW, 30,000 r/min bearingless permanent magnet motor with a fractional-slot concentrated winding for industrial compressor applications. A combined winding technique is used, where the same stator coils are able to produce suspension forces and torque as a means to increase the design performance. The final design is able support its rotor weight with only 2.5% of the slot current, has a maximum force error angle of 1.1° without requiring any stator skew, and a maximum efficiency of nearly 96%. Further efficiency improvements are achievable through techniques to reduce magnet losses (i.e., segmented magnets).

The optimization framework developed in this paper makes use of both structural and magnetic FEA solvers in combination with a DE algorithm. This is an improvement over bearingless design literature which often conducts a manual search of the design space. A set of objective variables and weighting factors are proposed. The optimization results are leveraged to study the sensitivity of the suspension force characteristics to changes in various design parameters. The paper shows that a stator geometry with no tooth tips (or minimal tooth tips) is preferred to obtain high suspension force performance characteristics. Future work on considering the magnet losses and cooling are proposed in order to obtain a practical prototype design.

REFERENCES

- [1] A. Chiba, T. Fukao, O. Ichikawa, M. Oshima, M. Takemoto, and D. Dorrell, *Magnetic Bearings and Bearingless Drives*. Newnes, 2005.
- [2] S.-L. Chen and C.-T. Hsu, "Optimal design of a three-pole active magnetic bearing," *IEEE Transactions on Magnetics*, vol. 38, no. 5, pp. 3458–3466, Sep 2002.
- [3] Y. Okada, N. Yamashiro, K. Ohmori, T. Masuzawa, T. Yamane, Y. Konishi, and S. Ueno, "Mixed flow artificial heart pump with axial self-bearing motor," *Mechatronics, IEEE/ASME Transactions on*, vol. 10, no. 6, pp. 658–665, Dec 2005.
- [4] W. Gruber, W. Amrhein, and M. Haslmayr, "Bearingless segment motor with five stator elements-design and optimization," *IEEE Transactions on Industry Applications*, vol. 45, no. 4, pp. 1301–1308, July 2009.

- [5] K. Raggl, T. Nussbaumer, and J. W. Kolar, "Comparison of separated and combined winding concepts for bearingless centrifugal pumps," *J. Power Electron.*, vol. 9, no. 2, pp. 243–258, 2009.
- [6] R. P. Jastrzebski, P. Jaatinen, H. Sugimoto, O. Pyrhnen, and A. Chiba, "Design of a bearingless 100 kw electric motor for high-speed applications," in *2015 18th International Conference on Electrical Machines and Systems (ICEMS)*, Oct 2015, pp. 2008–2014.
- [7] R. P. Jastrzebski, P. Jaatinen, O. Pyrhnen, and A. Chiba, "Design of 6-slot inset pm bearingless motor for high-speed and higher than 100kw applications," in *2017 IEEE International Electric Machines and Drives Conference (IEMDC)*, May 2017, pp. 1–6.
- [8] E. Severson and N. Mohan, "Bearingless motor system design for industrial applications," in *2017 IEEE International Electric Machines and Drives Conference (IEMDC)*, May 2017, pp. 1–8.
- [9] Y. Fu, M. Takemoto, S. Ogasawara, and K. Orikawa, "Investigation of a high speed and high power density bearingless motor with neodymium bonded magnet," in *Electric Machines and Drives Conference (IEMDC), 2017 IEEE International*. IEEE, 2017, pp. 1–8.
- [10] G. Munteanu, A. Binder, and T. Schneider, "Loss measurement of a 40 kw high-speed bearingless pm synchronous motor," in *2011 IEEE Energy Conversion Congress and Exposition*, Sept 2011, pp. 722–729.
- [11] C. Redemann, P. Meuter, A. Ramella, and T. Gempp, "30kw bearingless canned motor pump on the test bed," in *Seventh International Symp. on Magnetic Bearings, August 23-25, 2000, ETH Zurich*, 2000.
- [12] Y. g. Kang and E. L. Severson, "Optimization framework for a large, high speed bearingless permanent magnet motor," in *Sixteenth International Symposium on Magnetic Bearings*, August 2018, pp. 1–10.
- [13] R. P. Jastrzebski, P. Jaatinen, O. Pyrhnen, and A. Chiba, "Current injection solutions for active suspension in bearingless motors," in *2017 19th European Conference on Power Electronics and Applications (EPE'17 ECCE Europe)*, Sept 2017, pp. P.1–P.8.
- [14] E. L. Severson, R. Nilssen, T. Undeland, and N. Mohan, "Design of dual purpose no-voltage combined windings for bearingless motors," *IEEE Transactions on Industry Applications*, vol. 53, no. 5, pp. 4368–4379, Sept 2017.
- [15] E. Severson, "Bearingless motor technology for industrial and transportation applications," in *2018 IEEE Transportation Electrification Conference and Expo (ITEC)*, June 2018, pp. 1–8.
- [16] A. Chiba, K. Sotome, Y. Iiyama, and M. Azizur Rahman, "A novel middle-point-current-injection-type bearingless pm synchronous motor for vibration suppression," *Industry Applications, IEEE Transactions on*, vol. 47, no. 4, pp. 1700–1706, 2011.
- [17] H. Mitterhofer, B. Mrak, and W. Gruber, "Comparison of high-speed bearingless drive topologies with combined windings," *Industry Applications, IEEE Trans on*, vol. 51, no. 3, pp. 2116–2122, May 2015.
- [18] E. Severson, S. Gandikota, and N. Mohan, "Practical implementation of dual-purpose no-voltage drives for bearingless motors," *IEEE Transactions on Industry Applications*, vol. 52, no. 2, pp. 1509–1518, March 2016.
- [19] R. Amorim Torres and E. Severson, "Decoupled control for parallel drive no-voltage bearingless motors," in *Energy Conversion Congress and Exposition (ECCE), IEEE*, 2018, pp. 1–8.
- [20] D. Meeker, "Finite element method magnetics," *FEMM*, vol. 4, p. 32, 2010.
- [21] *Arnold 5 Non Grain Oriented Electrical Silicon Steel Core Loss Chart*, Arnold Magnetics, 2017.
- [22] J. An, A. Binder, and C. R. Sabirin, "Loss measurement of a 30 kw high speed permanent magnet synchronous machine with active magnetic bearings," in *Electrical Machines and Systems (ICEMS), 2013 International Conference on*. IEEE, 2013, pp. 905–910.
- [23] B. Riemer, M. Leßmann, and K. Hameyer, "Rotor design of a high-speed permanent magnet synchronous machine rating 100,000 rpm at 10kw," in *Energy Conversion Congress and Exposition (ECCE), 2010 IEEE*. IEEE, 2010, pp. 3978–3985.
- [24] A. Binder, T. Schneider, and M. Klohr, "Fixation of buried and surface-mounted magnets in high-speed permanent-magnet synchronous machines," *IEEE Transactions on Industry Applications*, vol. 42, no. 4, pp. 1031–1037, 2006.
- [25] F. Zhang, G. Du, T. Wang, G. Liu, and W. Cao, "Rotor retaining sleeve design for a 1.12-mw high-speed pm machine," *IEEE Transactions on Industry Applications*, vol. 51, no. 5, pp. 3675–3685, 2015.
- [26] A. Borisavljevic, H. Polinder, and J. Ferreira, "Enclosure design for a high-speed permanent magnet rotor," 2010.